








Hysteresis Current Control for Six-Phase Induction Motor Drives With Reduced Ripple and Improved Tracking Based on Subspace Decomposition and Restrained Voltage Vectors

Abdullah Shawier , Wessam E. Abdel-Azim , Alejandro G. Yepes , *Senior Member, IEEE*, Ayman Samy Abdel-Khalik , *Senior Member, IEEE*, Mostafa S. Hamad , *Senior Member, IEEE*, Shehab Ahmed , *Senior Member, IEEE*, and Jesús Doval-Gandoy , *Member, IEEE*

Abstract—Six-phase induction motor (6PIM) drives offer enhanced fault tolerance and reduced per-phase ratings. Hysteresis current control (HCC) is attractive for 6PIMs because it is simple, robust and fast. HCC is conventionally implemented so that each leg voltage is directly set based on the respective phase-current error. However, this approach does not consider that, in multiphase drives, phase voltages and currents are related through a combination of equivalent impedances corresponding to various subspaces. In general, there is a notable dissimilarity between these impedances, being typically small for secondary (xy) subspaces. This can cause large current distortion and poor reference tracking. This article proposes an improved HCC for 6PIM drives. Instead of directly inputting the per-phase current error to the hysteresis comparator and directly applying the switching states chosen by it, the input and output components associated with different subspaces are segregated. The input and output xy components are nullified in open loop so that the xy

impedance no longer affects the HCC behavior, even if low. This prevents the disrupting xy currents, ensures effective tracking of the torque/flux-producing $\alpha\beta$ reference current, and enables reconfiguration-less fault tolerance. Experiments using 6PIMs with different winding configurations corroborate the significant advantages of the proposal.

Index Terms—Current control, hysteresis control, multiphase motor drives, six-phase machines, winding configurations.

I. INTRODUCTION

THE interest in control techniques of multiphase drives can be traced back to several decades ago [1], [2]. Thanks to the rapid development of electric drives, multiphase machines have acquired a remarkable potential in many applications, such as electric vehicles, aircraft, and wind/marine turbines [3]. Multiphase drives offer important benefits, such as reduced rating for the switching devices and enhanced fault-tolerant capability [3]. To attain these features with high current quality and efficiency, a proper current control should be adopted. The existing control methods can be classified into two main groups: controllers based on pulsewidth modulation and direct controllers [4], [5], [6]. A typical example of the former is the field-oriented control (FOC) strategy using linear proportional-integral (PI) or proportional-resonant current control [7], [8], [9]. This option can provide a good current tracking with low total harmonic distortion (THD) [8], [9]. On the other hand, direct controllers exhibit advantages such as better dynamic response [4], [8], [10], [11] and the ability to easily handle nonlinear system constraints without windup problems [10], [11]. Hysteresis current control (HCC) [9], [12], [13], [14], [15], [16], [17], [18], [19], [20], [21], [22], [23], model predictive current control (PCC) [5], [6], [8], [24], [25], [26], [27], [28], and direct torque control [4] are some of the commonly used direct controllers [11]. HCC is arguably the simplest type of direct controller due to its easier implementation and the fact that it does not require any observer, parameter identification, prediction stage, or tuning of weighing factors [29], [30], [31]. Moreover, the independence from system parameters also allows high robustness [30], [31].

Manuscript received 8 December 2022; revised 18 April 2023 and 28 June 2023; accepted 17 August 2023. This work was supported in part by ITIDAS ITAC collaborative funded project under the category type of advanced research projects (ARP) and Grant ARP2020.R29.7, in part by the Government of Galicia under Grant ED431F 2020/07 and Grant GPC-ED431B 2020/03, in part by the Ministry of Science, Innovation and Universities under the Ramon y Cajal Grant RYC2018-024407-I, and in part by Spanish State Research Agency (AEI) under project PID2022-136908OB-I00/AEI. (Corresponding author: Jesús Doval-Gandoy.)

Abdullah Shawier, Wessam E. Abdel-Azim, and Ayman Samy Abdel-Khalik are with the Electrical Engineering Department, Faculty of Engineering, Alexandria University, Alexandria 21544, Egypt (e-mail: abdullah.shawier@alexu.edu.eg; wessam.essam@alexu.edu.eg; ayman.abdel-khalik@alexu.edu.eg).

Alejandro G. Yepes and Jesús Doval-Gandoy are with the Applied Power Electronics Technology Research Group, CINTECX, Universidade de Vigo, 36310 Vigo, Spain (e-mail: agyepes@uvigo.es; jdoval@uvigo.es).

Mostafa S. Hamad is with the Research and Development Center, Arab Academy for Science, Technology and Maritime Transport, Al Alamein 51718, Egypt (e-mail: mostafa.hamad@staff.aast.edu).

Shehab Ahmed is with the CEMSE Division, King Abdullah University of Science and Technology, Thuwal 23955, Saudi Arabia (e-mail: shehab.ahmed@kaust.edu.sa).

Color versions of one or more figures in this article are available at <https://doi.org/10.1109/TIE.2023.3308136>.

Digital Object Identifier 10.1109/TIE.2023.3308136

HCC was originally applied to three-phase drives based on FOC, and it was later extended to multiphase ones [12], where it soon became popular due to the aforesaid advantages [9], [12], [13], [14], [15], [16], [17], [18], [19], [20], [21], [22], [23]. The conventional HCC for multiphase drives uses the phase-current error as input, not the error expressed in the so-called vector-space-decomposition (VSD) subspaces, the latter of which is often adopted for other kinds of controllers [11]. This is true for HCC even in some cases where the current references are generated in the VSD subspaces, which can be convenient, e.g., if the torque is regulated through the synchronous dq currents within the VSD fundamental ($\alpha\beta$) plane [9], [12], [14], [22] or if the current constraints due to open-phase faults are expressed in these coordinates [9]. With this approach, after the current references are generated, they are transformed into their phase quantities using the inverse VSD transform. Subsequently, they are compared with the measured currents, and then the resulting per-phase errors are fed to the HCC to generate the switch firing signals [9], [23], similarly to the conventional three-phase HCC. There are also other publications in which the current references are obtained from the torque reference and position directly in phase coordinates, so that no VSD transformation is required before the per-phase HCC [15], [17], [19], [20], [21]. The existing literature has shown that the HCC may be used in many different conditions, including open-phase faults [9], [12], [13], [14], [15], [16], [17], [18], [19], [20], [21], [22], either induction [9], [12], [23] or permanent-magnet synchronous machines (PMSMs) [13], [14], [15], [16], [17], [18], [19], [20], [21], [22], different types of stator winding distribution [18] or stator phase connections [19], [20], nonsinusoidal current references [13], [14], [15], [17], [19], [20], [21], or various phase numbers such as five [9], [12], [13], [14], [15], [17], [18], [19], [20], [21], six [22], nine [23], or 15 [16].

However, HCC is known to cause substantial current ripple in multiphase drives [9]. To the authors' knowledge, barely any solutions have been proposed to mitigate this disadvantage of the HCC in multiphase machines. In fact, in most of the publications using HCC for multiphase drives, no improvements or modifications are applied to the HCC, and it is just used as a tool to validate contributions on other aspects (e.g., current references). In [22], a technique that overcomes the problem of variable switching frequency of the conventional HCC is presented for a PMSM with an asymmetrical six-phase (A6) winding. With this method [22], fixed switching frequency is obtained and the current distortion is attenuated, but dependence on several parameters is introduced.

Customarily, HCC is conceived under the implicit assumption that the voltage of each phase is just related to the current of the corresponding phase, through a simple first-order linear equation [22], without considering the impedance mismatch that may exist between different VSD subspaces. This simplification is related to the aforementioned facts that the phase-current error is directly used as input of the HCC and that the HCC directly sets the corresponding leg voltage. However, in practice, the impedance of each subspace depends on the winding design, which can yield a notable discrepancy between the machine equivalent parameters of the various subspaces [25].

In particular, the impedance in the secondary (xy) subspaces is normally very small [1]. Increasing it by special winding distributions (e.g., chording) could mean making the leakage inductances greater (reducing the achievable torque) [25] or introducing undesired flux harmonics (e.g., even-order ones for chorded symmetrical winding) [32]. It is known that the low xy impedance tends to give rise to large xy currents, e.g., when using PCC [6], [25]. This could also help explain the large current distortion reported for HCC in multiphase drives in previous publications [9]. Nonetheless, since the subspace impedance dissimilarity violates the aforesaid underlying assumption of HCC, it may not only affect the current ripple magnitude but also disturb the proper simultaneous tracking of the fundamental- and secondary-subspace current components, even if the references for the latter are set to zero. In the literature, there is no practical solution to control each VSD subspace separately using HCC, which can be especially important when there is a significant mismatch between the subspace impedances. Very recently, a hybrid HCC-PCC method using VSD has been presented [33], but it relies on the knowledge of the machine parameters, conversely to pure HCC.

In this context, this article proposes a novel technique to enhance the performance of HCC for six-phase induction motors (6PIMs). The subspace components of the HCC inputs and outputs are decomposed and they are suitably handled so that the xy equivalent circuit is removed from the plant model seen by the HCC, to avoid its troublesome effects. In particular, the inverter voltage vector (VV) is selected so that it is close to the hysteresis original output but without exciting the xy plane. The xy components of the input current error are also discarded, preventing their disruptive impact. Consequently, the current distortion and reference tracking are greatly improved. Moreover, in the case of an open-phase fault, the fact that the HCC does not act on the xy plane permits the xy currents to naturally adapt to the postfault constraints, providing reconfiguration-less tolerance. The proposed method does not require the knowledge of any system parameters. 6PIMs with different winding layouts are employed to experimentally validate the proposed HCC under healthy conditions and single open-phase faults. Extensive comparison with other controllers is included.

The rest of this article is organized as follows. The machine modeling and the mapping of the inverter VVs are described in Section II. The proposed HCC is presented in Section III. The experimental results are discussed in Section IV. Finally, Section V concludes this article.

II. VSD MODEL OF A 6PIM DRIVE

A model is given next for 6PIMs with two three-phase winding sets. As shown in Fig. 1, these two sets have an angle δ between them, which is $\pi/3$ and $\pi/6$ for symmetrical six-phase (S6) and A6, respectively [34]. Furthermore, the VSD mapping of the inverter VVs is discussed for S6 and A6. The 6PIM is assumed to have two isolated neutral

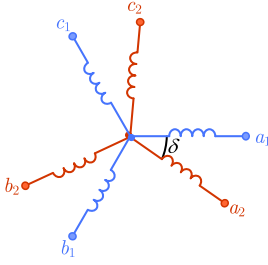


Fig. 1. Layout of six-phase winding configurations with arbitrary angle δ .

points, which is convenient to avoid zero-sequence circulating currents.

A. 6PIM Modeling

The VSD transform for each winding type (δ value) is as follows [34]:

$$\mathbf{T} = \frac{1}{3} \begin{bmatrix} 1 & c(\gamma) & c(2\gamma) & c(\delta) & c(\delta + \gamma) & c(\delta + 2\gamma) \\ 0 & s(\gamma) & s(2\gamma) & s(\delta) & s(\delta + \gamma) & s(\delta + 2\gamma) \\ 1 & c(2\gamma) & c(\gamma) & -c(\delta) & -c(\delta + \gamma) & -c(\delta + 2\gamma) \\ 0 & s(2\gamma) & s(\gamma) & s(\delta) & s(\delta + \gamma) & s(\delta + 2\gamma) \\ 1 & 1 & 1 & 0 & 0 & 0 \\ 0 & 0 & 0 & 1 & 1 & 1 \end{bmatrix} \quad (1)$$

where c and s are cosine and sine, respectively, and $\gamma = 2\pi/3$. Then, an array $\mathbf{U}_{a_1-c_2}$ formed by the phase components a_1-c_2 of any variable u may be transformed to VSD coordinates as

$$\mathbf{U}_{\alpha\beta xy z_1 z_2} = \mathbf{T} \mathbf{U}_{a_1-c_2} \quad (2)$$

where

$$\mathbf{U}_{a_1-c_2} = [u_{a_1} \ u_{b_1} \ u_{c_1} \ u_{a_2} \ u_{b_2} \ u_{c_2}]^T \quad (3)$$

$$\mathbf{U}_{\alpha\beta xy z_1 z_2} = [u_\alpha \ u_\beta \ u_x \ u_y \ u_{z_1} \ u_{z_2}]^T. \quad (4)$$

Using VSD, the stator 6PIM model can be expressed in the $\alpha\beta$ plane as for a three-phase motor [1], [24]; e.g., as [35]

$$\mathbf{V}_{\alpha\beta} = R^s \mathbf{I}_{\alpha\beta} + \sigma L_{\alpha\beta}^s \frac{d}{dt} \mathbf{I}_{\alpha\beta} + \frac{L_{\alpha\beta}^m}{L_{\alpha\beta}^r} \frac{d}{dt} \mathbf{\Lambda}_{\alpha\beta}^r \quad (5)$$

where R^s is the stator resistance, $L_{\alpha\beta}^s = L_{\alpha\beta}^{ls} + L_{\alpha\beta}^m$ and $L_{\alpha\beta}^r = L_{\alpha\beta}^{lr} + L_{\alpha\beta}^m$ are the stator and rotor self-inductances, respectively, $L_{\alpha\beta}^{ls}$ and $L_{\alpha\beta}^{lr}$ are the $\alpha\beta$ stator and rotor leakage inductances, respectively, $L_{\alpha\beta}^m$ is the magnetizing inductance, $\sigma L_{\alpha\beta}^s = (1 - (L_{\alpha\beta}^m)^2 / (L_{\alpha\beta}^s L_{\alpha\beta}^r)) L_{\alpha\beta}^s$ is the stator transient inductance and

$$\mathbf{V}_{\alpha\beta} = [v_\alpha \ v_\beta]^T; \mathbf{I}_{\alpha\beta} = [i_\alpha \ i_\beta]^T; \mathbf{\Lambda}_{\alpha\beta}^r = [\lambda_\alpha^r \ \lambda_\beta^r]^T \quad (6)$$

where v and i represent stator voltage and current, respectively, and λ^r is the rotor flux linkage.

Since the coupling with the rotor through the xy space harmonics is usually negligible [36], the stator model in the xy

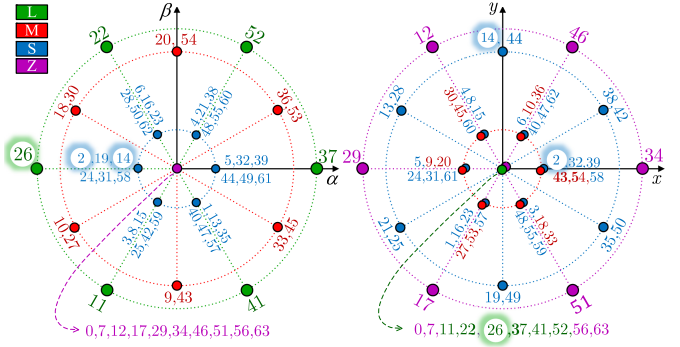


Fig. 2. Inverter VV mapping in the $\alpha\beta$ (left) and xy (right) planes for S6.

plane is as follows [1], [24]:

$$\mathbf{V}_{xy} = R^s \mathbf{I}_{xy} + L_{xy}^{ls} \frac{d}{dt} \mathbf{I}_{xy} \quad (7)$$

where L_{xy}^{ls} is the xy stator leakage inductance, and

$$\mathbf{V}_{xy} = [v_x \ v_y]^T; \mathbf{I}_{xy} = [i_x \ i_y]^T. \quad (8)$$

It can be observed in (5) and (7) that the xy impedance is just given by the stator resistance and leakage inductance, whereas the $\alpha\beta$ one is increased to a considerable extent by the coupling with the rotor circuit [1], i.e., normally $\sigma L_{\alpha\beta}^s \approx L_{\alpha\beta}^{ls} + L_{\alpha\beta}^{lr}$ is substantially larger than L_{xy}^{ls} .

B. Two-Level Six-Phase Inverter Modeling

For a two-level voltage-source inverter, the phase voltages can be found from the leg switching states as follows [24], [28]:

$$\mathbf{V}_{a_1-c_2} = \frac{v_{dc}}{3} \begin{bmatrix} 2 & -1 & -1 & 0 & 0 & 0 \\ -1 & 2 & -1 & 0 & 0 & 0 \\ -1 & -1 & 2 & 0 & 0 & 0 \\ 0 & 0 & 0 & 2 & -1 & -1 \\ 0 & 0 & 0 & -1 & 2 & -1 \\ 0 & 0 & 0 & -1 & -1 & 2 \end{bmatrix} \begin{bmatrix} S_{a_1} \\ S_{b_1} \\ S_{c_1} \\ S_{a_2} \\ S_{b_2} \\ S_{c_2} \end{bmatrix} \quad (9)$$

where v_{dc} is the dc-link voltage and $S_k \in \{0, 1\}$ is the switching state of leg k . There are 64 switching states for the inverter. These states map as 64 VVs in each VSD subspace, which may be found by means of (2).

Figs. 2 and 3 show for S6 and A6, respectively, the projections of the switching states as VVs in the $\alpha\beta$ and xy planes [6], [24], [25]. The VVs are classified into four subsets for S6 depending on their $\alpha\beta$ magnitude: large (L), medium (M), small (S), and zero (Z) VVs. On the other hand, the A6 has an additional subset known as medium-large (ML). The VVs of each subset differ for S6 and A6. The VV magnitudes from largest to smallest in both planes for S6 are 0.67, 0.57, 0.33, and 0 p.u.; for A6, they are 0.64, 0.47, 0.33, 0.17, and 0 p.u.. The naming of the VVs is defined using the binary representation $S_{a_1-c_2}$ of the corresponding switching states, with the binary digits being sorted from most to least significant, following the same phase order as in the right-hand side of (9) from top to bottom. For instance,

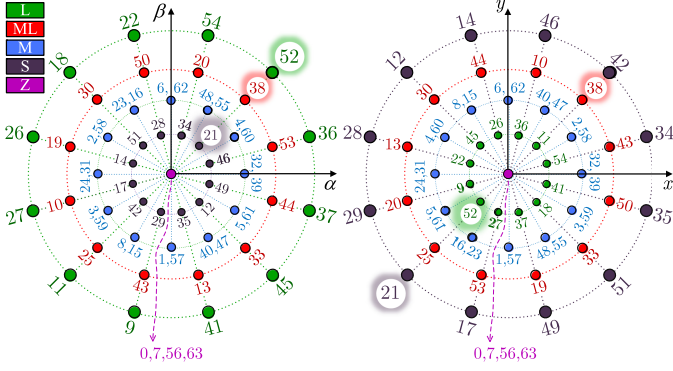


Fig. 3. Inverter VV mapping in the $\alpha\beta$ (left) and xy (right) planes for A6.

the state 14 corresponds to the switching pattern 001110 in all subspaces. The particular VVs highlighted in Figs. 2 and 3 will be used later to illustrate some examples.

III. PROPOSED HCC

As mentioned earlier, HCC is a direct controller often used for three-phase and multiphase drives, due to its simplicity, robustness, and fast response [9], [12], [13], [14], [15], [16], [17], [18], [19], [20], [21], [22], [23], [29], [30]. Compared with three-phase drives, the effectiveness of the conventional HCC may be more compromised in multiphase ones. This is because the conventional HCC relies on the assumption that voltages and currents are related by a single pure inductance [22], [30], [31], but in a multiphase machine, the $\alpha\beta$ and xy impedances [see (5) and (7)] can be very different [6], [25]. Thus, the assumption of a pure inductance is far from true. For example, if the output VV for S6 at a certain instant is 11 (see Fig. 2), which corresponds to $S_{a_1-c_2} = 001011$ and has zero xy contribution, a small change in i_{a_2} , i_{b_2} and i_{c_2} may cause the VV to switch to 12 ($S_{a_1-c_2} = 001100$), producing a very large xy current. This disruptive current is also reflected in the phase currents used as inputs of the HCC, disturbing the $\alpha\beta$ reference tracking in the following sampling periods as well. As will be shown in the results, the HCC behavior is actually quite poor when there is a significant dissimilarity between the $\alpha\beta$ and xy inductances, such as what happens for unchorded S6 and chorded A6 6PIMs, where the reduced flux harmonics and total (stator plus rotor) leakage inductances (allowing higher torque), respectively, are accompanied by very small xy inductance [25], [32].

The enhanced HCC proposed here to overcome this problem is illustrated by the red-shaded area in Fig. 4, in the context of a 6PIM drive using FOC. References are denoted by an asterisk. The novel HCC is based on decomposing the input error as well as the hysteresis output VV by using the VSD. In this manner, the components of these signals can be treated differently in each VSD subspace, which corresponds to specific machine parameters [see (5) and (7)]. In particular, the xy terms, usually associated with much lower impedance, are removed to avoid their disruptive effect. This differs from the conventional multiphase HCC [9], [12], [13], [14], [15], [16], [17], [18], [19],

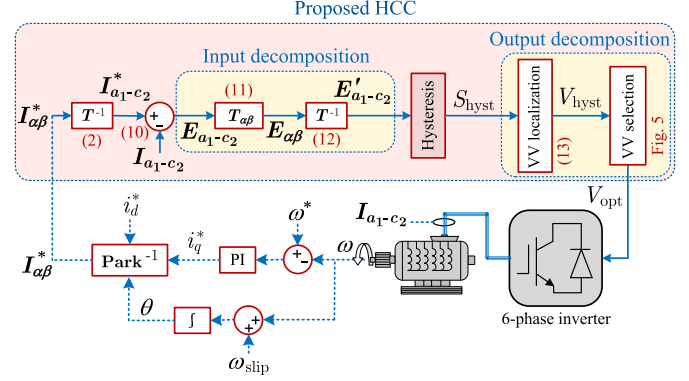


Fig. 4. Overall block diagram of a 6PIM drive based on FOC and the proposed HCC (red-shaded area).

[20], [21], [22], [23], where neither the input nor the output decomposition is applied. Although the VSD is frequently used for other direct current controllers such as those based on PCC [6], [25], the proposed HCC is advantageous in simplicity, thanks to the lack of observer and prediction stages, weighting factors, and of course, of evaluating all the existing VVs.

In Fig. 4, the proposed HCC consists of several main stages: input error decomposition, hysteresis comparison, and output VV decomposition, with the last one comprising the hysteresis VV localization and the optimum VV selection. The $\alpha\beta$ current reference $I_{\alpha\beta}^*$ is obtained beforehand (bottom left corner of Fig. 4) by applying the inverse rotational Park transform to the d - and q -axes references i_d^* and i_q^* , set to yield certain flux and torque, respectively; the latter may be adjusted by a speed PI controller, as in standard indirect rotor FOC [7]. Similarly to conventional HCC [23], $I_{\alpha\beta}^*$ is then transformed into phase components $I_{a_1-c_2}^*$ by using the inverse VSD transform T^{-1} according to (2), as depicted in the left-hand side of Fig. 4. Next, the array of six phase-current errors is obtained by subtracting the measured phase currents from the respective references as

$$E_{a_1-c_2} = I_{a_1-c_2}^* - I_{a_1-c_2} \quad (10)$$

and then, unlike in the conventional HCC, its $\alpha\beta$ components are extracted by using the first two rows of T , i.e., $T_{\alpha\beta}$, while avoiding the other VSD components (rows):

$$E_{\alpha\beta} = [e_\alpha \ e_\beta]^T = T_{\alpha\beta} E_{a_1-c_2}. \quad (11)$$

Afterward, the $\alpha\beta$ error $E_{\alpha\beta}$ is used alone to reconstruct a set of six phase-current errors $E'_{a_1-c_2}$ with only $\alpha\beta$ content, by using the inverse of T :

$$E'_{a_1-c_2} = T^{-1} \begin{bmatrix} E_{\alpha\beta} \\ e_\alpha \ e_\beta \ 0 \ 0 \ 0 \ 0 \end{bmatrix}^T. \quad (12)$$

If the product between T^{-1} and $T_{\alpha\beta}$ (filling with zeros the third-sixth $T_{\alpha\beta}$ rows) is computed offline, then $E'_{a_1-c_2}$ can be obtained online from $E_{a_1-c_2}$ with at most 36 multiplications and 30 additions. Most importantly, it should be remarked that the rows of T related to VSD subspaces other than $\alpha\beta$ [see (1)–(3)] have been dropped in $T_{\alpha\beta}$ to remove those disruptive VSD components from the current error through (11), in order to prevent

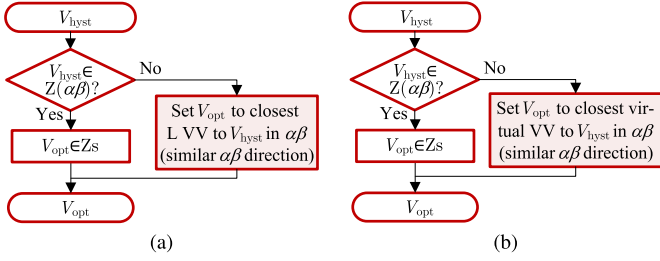


Fig. 5. Representation of the algorithm for the optimum VV selection of the proposed HCC (last block of the red-shaded area in Fig. 4), which may be implemented by a lookup table. (a) S6. (b) A6.

them from affecting the HCC behavior. Indeed, the modified phase-current error $E'_{a_1-c_2}$ in (12) only contains terms associated with the $\alpha\beta$ plane.

Subsequently, the reconstructed error $E'_{a_1-c_2}$ is fed to the hysteresis comparator to obtain its output switching state vector in phase coordinates S_{hyst} , which is one of the possible 64 switching states of the inverter. The corresponding VV V_{hyst} is identified (among those from Figs. 2 and 3) in the localization stage by simply computing the decimal number associated with the S_{hyst} binary code:

$$V_{hyst} = 2^5 S_{a_1} + 2^4 S_{b_1} + 2^3 S_{c_1} + 2^2 S_{a_2} + 2 S_{b_2} + S_{a_2}. \quad (13)$$

This only involves five multiplications and five additions. Finally, in the VV selection stage, which is represented in Fig. 5, the proposed algorithm limits the choice of the optimum output VV V_{opt} to a certain VV set. This process can be simply applied by a lookup table, with the V_{hyst} VV number as input and the optimum V_{opt} as output. If V_{hyst} is one of the VVs that is Z in the $\alpha\beta$ plane [i.e., $V_{hyst} \in Z(\alpha\beta)$], then V_{opt} is set to one of the zero-sequence VVs (now denoted as Zs), which are the four VVs that have zero magnitude in both $\alpha\beta$ and xy planes. Otherwise, V_{opt} is selected so as to contribute actively to the $\alpha\beta$ plane while keeping a null impact on the xy plane, which is achieved differently depending on whether the machine is of S6 or A6 type, as discussed next.

For S6 [see Fig. 5(a)], only the L subset is considered in the VV selection, to maximize the dc-link utilization and reduce the xy content. Indeed, in Fig. 2, the L subset (green) has maximum and zero magnitudes in the $\alpha\beta$ and xy planes, respectively. Namely, the L VV that is closest to V_{hyst} in the $\alpha\beta$ plane (similar direction) is selected as V_{opt} , to achieve a good $\alpha\beta$ current tracking. For instance, referring to Fig. 2, if S_{hyst} results in the VVs with numbers 2 or 14, the algorithm finds that the nearest L VV in the $\alpha\beta$ plane is 26, which has zero magnitude in the xy plane, and sets V_{opt} to it.

For the A6 case [see Fig. 5(b)], the method limits the selection of the output VV to the synthesized virtual VV set shown in Fig. 6. The virtual VVs are synthesized from the L and ML subsets as done in [27], [28] for PCC. These virtual VVs have zero magnitude in the xy plane, and hence they produce zero xy current [5], [27], similarly to the L subset for S6. Their $\alpha\beta$ magnitude is 0.59 p.u.. For instance, if the V_{hyst} number is 21 (see Fig. 3), the closest L and ML VVs (similar $\alpha\beta$ direction)

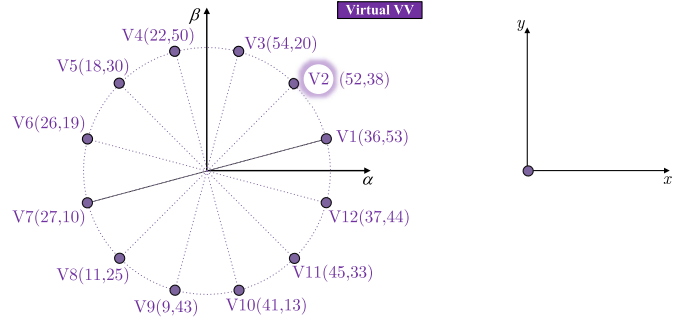


Fig. 6. Mapping of the virtual VVs in the $\alpha\beta$ (left) and xy (right) planes for A6.

TABLE I
COMMON PARAMETERS OF THE PROTOTYPE MACHINES

Parameter	S6/A6
Number of poles	4
Rated frequency (Hz)	50
Rated power (kW)	1.1
Rated rms phase current (A)	2.8
Rated rms phase voltage (V)	110
Rated speed (r/min)	1400

are 38 and 52, which have opposite directions in the xy plane; accordingly, the algorithm selects for V_{opt} the virtual VV from Fig. 6 that combines these two VVs (i.e., V2) so that the xy magnitude is canceled.

It is worth highlighting that, since the xy components of the HCC input and output are canceled in this manner for both S6 and A6, the fact that the xy impedance is normally much lower than the $\alpha\beta$ one does not affect the behavior of the proposed controller. The HCC has been effectively modified so that only the $\alpha\beta$ equivalent circuit is seen by it, removing the xy plane from its plant model, and hence making it more similar to that of a three-phase machine. Thus, the performance can be expected to be much closer to the ideal one than when using the conventional HCC. Additionally, the absence of xy closed-loop control makes it possible to obtain reconfiguration-less tolerance to open-phase faults, since the postfault coupling between the $\alpha\beta$ and xy planes no longer means a conflict for the controller, similarly to what happens with PCC [28].

IV. EXPERIMENTAL RESULTS

Two prototype (chorded and unchorded) 12-phase machines, designed to be connected externally as 6PIMs with different winding layouts [25], [36], are used. The parameters are shown in Tables I and II, based on [25], [36]. Fig. 7 shows the system setup. Two three-phase inverter power modules IGCM20F60GA are used to construct the six-leg inverter, controlled by a dSPACE-DS1202-MicroLabBox digital platform. The inverter dc link is fed by a 300-V 11-A programmable dc source. A dc generator with a bank of variable resistors is coupled to the 6PIM, acting as a mechanical load. The phase-current and the rotor-speed measurements are obtained by means of six LA-55P-LEM Hall-effect current sensors and an incremental

TABLE II
RESISTANCE AND INDUCTANCE VALUES OF THE PROTOTYPE MACHINES

Parameter	Symbol	Unchorded		Chorded	
		S6	A6	S6	A6
Stator resistance (Ω)	R_s	5.00	5.00	4.18	4.18
Rotor resistance (Ω)	R_r	2.90	3.10	3.46	3.67
$\alpha\beta$ stator leakage inductance (mH)	$L_{\alpha\beta}^{ls}$	10.0	9.60	9.10	12.0
$\alpha\beta$ rotor leakage inductance (mH)	$L_{\alpha\beta}^{lr}$	21.0	22.5	19.1	16.7
$\alpha\beta$ magnetizing inductance (mH)	$L_{\alpha\beta}^m$	284	304	260	247
xy stator leakage inductance (mH)	L_{xy}^{ls}	4.52	25.5	11.8	7.50

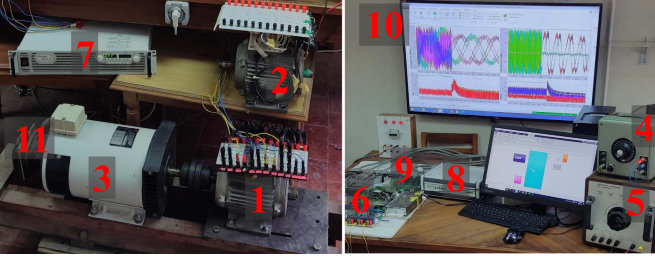


Fig. 7. Experimental setup with 1) chorded and 2) unchorded 6PIMs, 3) dc generator with 4) its dc excitation and 5) loading resistor, 6) six-phase inverter, 7) dc-link supply, 8) real-time system (dSPACE 1202 MicroLabBox) and its 9) interface board, 10) host PC (ControlDesk), and 11) encoder.

E6B2-CWZ1X encoder, respectively. The dc-link voltage v_{dc} is 300 V. The reference d -axis current i_d^* is 1.41 A. Unless otherwise stated, the tests are performed using the unchorded S6 and chorded A6 configurations, which have low xy inductances (see Table II) [25].

The overall control scheme is in accordance with Fig. 4 for testing the proposed HCC. The input and output decomposition stages are removed for the conventional HCC. Note that the reference currents for the secondary subspaces are zero, although for the proposed HCC they are ignored through (11). The dSPACE sampling period is $25 \mu\text{s}$ in all cases of HCC except when using virtual VVs for A6 with the proposed HCC, where two VVs per sampling period are applied, and hence it is increased to $50 \mu\text{s}$.

First, the steady-state waveforms of the measured and reference currents are presented during eight cycles for S6 and A6 in Figs. 8 and 9, respectively, using the conventional and proposed HCC. The reference values of speed and dq current $|i_{dq}^*|$ (load) are set to rated. Current signals are shown rather than voltage ones because the former are more closely related to the machine performance in terms of torque, flux, and losses. The reference and estimated torque are also included. The first two cycles are obtained using the conventional HCC in a healthy scenario. Then, the HCC is replaced by the proposed one to evaluate its performance in both healthy (initially) and faulty (following two cycles) conditions. Finally, the conventional HCC is enabled under the open-phase fault. It should be noted that these four situations are tested separately and presented consecutively in these figures for compactness and for facilitating the comparison.

From the first two cycles of Figs. 8 and 9, it is obvious that the conventional HCC fails to track the $\alpha\beta$ -current and

torque references and, especially, to provide zero xy current. This results in a significant distortion in the phase currents. As aforesaid, this behavior may be explained by the fact that the $\alpha\beta$ and xy impedances are unequal, with the latter being very small. Concerning, the second pair of two cycles from Figs. 8 and 9, where the proposal is activated, it can be seen that the improvement is considerable, both in terms of reference tracking and a small current ripple. The proper tracking of the $\alpha\beta$ current/torque and the xy current cancellation can be mainly attributed to the input and output decomposition stages from Fig. 4, respectively. Then, the following two cycles of Figs. 8 and 9 confirm that the proposed HCC is able to work properly under a single open-phase fault without control reconfiguration. Indeed, a good tracking of the $\alpha\beta$ current/torque is kept, while the x current (not controlled in a closed loop) naturally adapts to the postfault current constraint ($i_x = -i_\alpha$ [28], [37]), as happens for fault-tolerant reconfiguration-less PCC [28]. The magnitude of the $\alpha\beta$ current reference is deliberately reduced under the fault to ensure that none of the phase currents exceeds 1 p.u. [34]. Finally, it can be observed in the last two cycles of Figs. 8 and 9 that in a faulty case, the conventional HCC performs even worse than in a healthy scenario, with extremely large error and distortion, unlike the proposal.

Some figures of merit are provided in Table III for healthy rated conditions: THD of the phase currents, mean squared error (MSE) of the $\alpha\beta$ currents, average switching frequency f_{sw} , maximum and minimum per-leg instantaneous switching frequency, maximum instantaneous (per-sample) phase-voltage change Δv [using (9)], settling time for i_q^* step [10],¹ and current-control execution time. Besides the conventional and proposed HCC, other kinds of current control are also included for comparison: dq -frame PI [38] and finite-control-set model PCC [6], [28]. The PI control is designed according to [38], using conventional carrier-based pulsewidth modulation (PWM) with double zero-sequence injection [39] and PWM frequency of 5 kHz. For PCC, the VVs under consideration [6], [28] and the sampling period are as for HCC. Chiefly, Table III confirms the most important outcome from Figs. 8 and 9, i.e., that the proposed HCC reduces to a great extent the current distortion (i.e., THD) and tracking error (i.e., MSE) with respect to the conventional HCC. These parameters are also better with the proposed HCC than for PI PWM control, because of the large xy switching ripple of the latter, which does apply VVs with nonzero xy projection. Regarding \bar{f}_{sw} , for the S6 it is similar for both kinds of HCC, whereas it rises when the proposal is tested with A6. The latter occurs because, although the output VV when using the proposed HCC is repeated for many consecutive sampling periods (73.2% of the time for S6 and 65.7% for A6), for A6 the use of virtual VVs in these cases implies switching between two VVs. It may also be pointed out that \bar{f}_{sw} (and hence, switching loss) with the proposed HCC is kept reasonably low because the VVs are adjacent during 12.8% and 11.6% of the samples for S6 and A6, respectively, which is very close to the percentage of samples in which the VVs are not repeated:

¹A tolerance band of 12% is used for the settling time, taking into account the switching ripple.

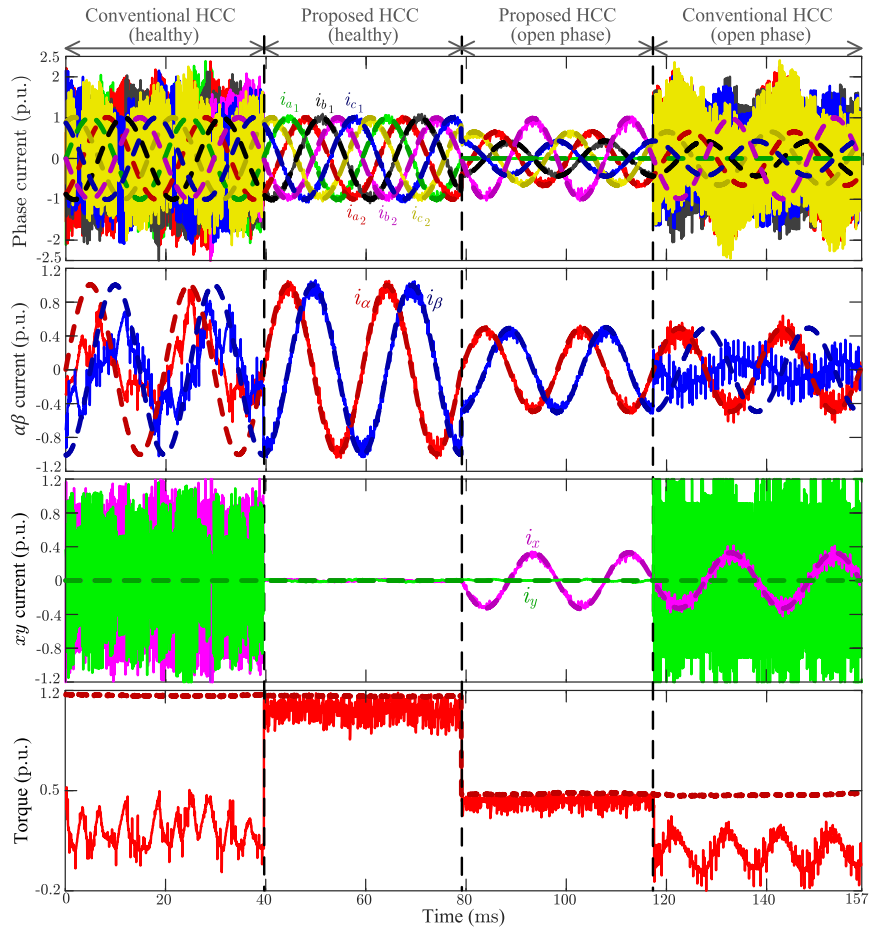


Fig. 8. Steady-state reference (dark dashed) and measured/estimated (bright solid) currents/torque for S6 at 1400 r/min. From left to right: conventional HCC with healthy drive, proposed HCC with healthy drive, proposed HCC with phase a_1 open, and conventional HCC with phase a_1 open.

TABLE III
COMPARISON OF FIGURES OF MERIT OF THE CURRENT CONTROLLERS AT RATED CONDITIONS

Parameter	Unchorded S6				Chorded A6			
	PI	PCC	Conv. HCC	Prop. HCC	PI	PCC	Conv. HCC	Prop. HCC
Current THD (%)	47.2	6.8	222.3	9.4	21.3	10.8	130.5	13.0
MSE $_{\alpha\beta}$ (%)	0.16	0.37	21.86	0.38	0.06	0.38	9.65	0.88
MSE $_{xy}$ (%)	4.97	0.02	79.17	0.02	0.96	0.13	37.16	0.14
Max. f_{sw} (kHz)	5.0	20	20	20	5.0	20	20	20
\bar{f}_{sw} (kHz)	5.0	2.0	3.8	2.0	5.0	6.6	4.0	7.0
Min. f_{sw} (kHz)	5.0	0.19	0.28	0.24	5.0	0.15	0.37	0.71
Max. Δv (V)	200	400	400	400	200	400	400	400
i_q settling time (ms)	2.0	0.27	∞	0.25	1.6	0.28	∞	0.27
Execution time (μs)	1.3	1.6	0.6	0.9	1.3	1.9	0.6	1.0
Requires machine parameters	Yes	Yes	No	No	Yes	Yes	No	No

26.8% and 34.3%, respectively. As for Δv , it is $4v_{dc}/3$ for all methods except for PI, for which it is halved. Concerning the transient behavior, it can be seen in Table III and Fig. 10 that the proposed HCC attains a much shorter settling time than PI PWM, as expected.² The performance of the new HCC is very similar to that of PCC in most aspects, but the proposal does not

²As a side note, the greater low-frequency ripple in Fig. 10(a) for PI control is due to drive nonlinearities, whose effect is better rejected by the other methods. The fifth and seventh harmonics are mapped into the $\alpha\beta$ (dq) plane for S6 and not for A6 [40, eq. (3)]. This ripple barely affects the settling time.

rely on the machine parameters and it consumes less execution time, despite being slightly longer than for the conventional HCC (see Table III). The considerable computational burden of PI control is mainly due to the rotational transforms, which include trigonometric functions. In summary, the proposed HCC ensures principally small current error and distortion (unlike conventional HCC), as well as moderate switching frequency, fast response (unlike PI), and relatively short execution time without knowledge of machine (or other) parameters (unlike PCC).

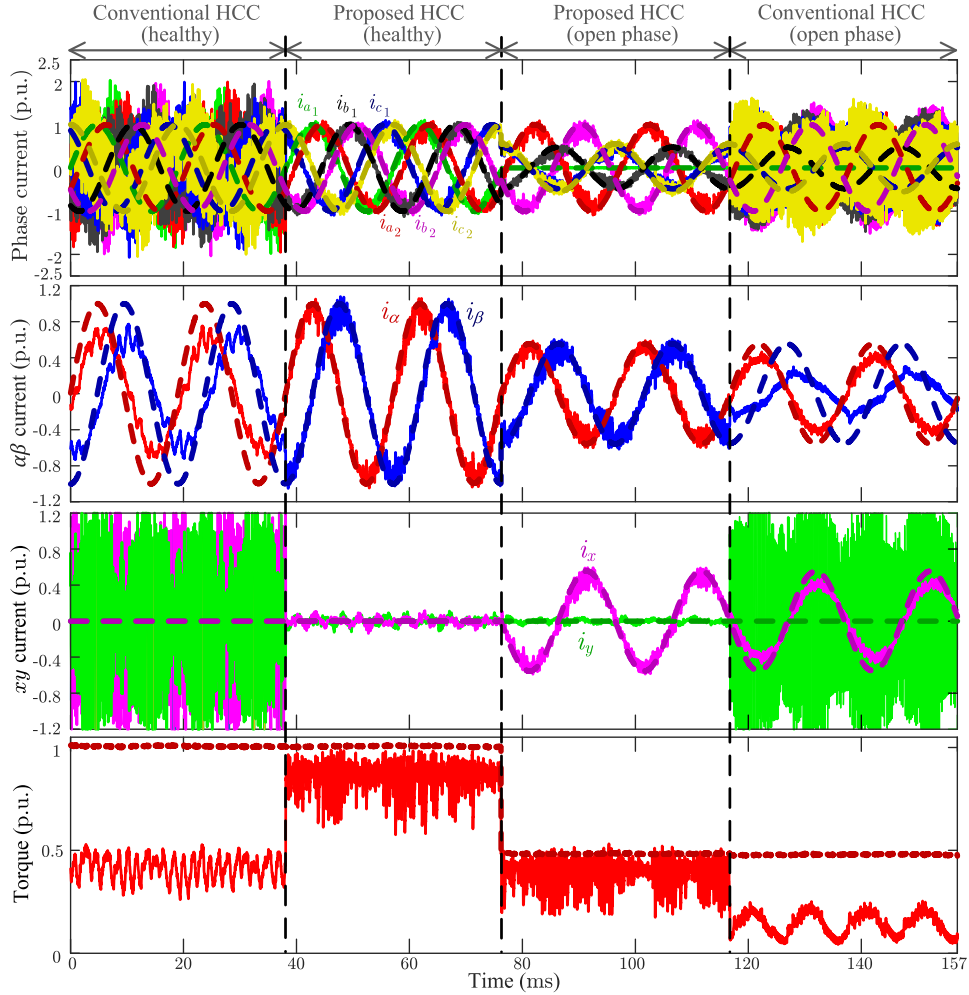


Fig. 9. Steady-state reference (dark dashed) and measured/estimated (bright solid) currents/torque for A6 at 1400 r/min. From left to right: conventional HCC with healthy drive, proposed HCC with healthy drive, proposed HCC with phase a_1 open, and conventional HCC with phase a_1 open.

For the sake of completeness, the plots of current THD at $|i_{dq}^*|$ load values of 0.4 p.u. and 1.0 p.u. and at other speeds when using the conventional and proposed HCC are provided in Fig. 11(a) and (b), respectively. The THD of the conventional HCC at $|i_{dq}^*| = 0.4$ p.u. is not included because the machine does not run in that case, due to its large dq error. In addition, \bar{f}_{sw} for the proposed HCC is also shown in the full speed range in Fig. 12. Most importantly, these figures corroborate that the main aforesaid conclusions about the THD and \bar{f}_{sw} also hold in other conditions. Namely, although the THD increases to some extent at low speed, it is always much lower for the proposed HCC than for the conventional HCC. The \bar{f}_{sw} value is acceptable (low) for the proposal, even though it is higher for A6 because of the use of virtual VVs.

The proposed HCC, combined with outer speed PI control (see Fig. 4), is tested under a load or speed-reference step, as shown in Figs. 13 and 14, respectively, for both S6 and A6.³ Effective current and speed tracking is achieved. Note that, although there

³The limit of the i_q^* value at the output of the speed control is set slightly lower for A6 because of the greater current distortion for A6 (see Table III).

TABLE IV
COMPARISON OF FIGURES OF MERIT OF THE CURRENT CONTROLLERS FOR MACHINES WITH HIGH L_{xy}^{LS} AT RATED CONDITIONS

Parameter	Chorded S6		Unchorded A6	
	Conv. HCC	Prop. HCC	Conv. HCC	Prop. HCC
Current THD (%)	23.2	17.8	9.1	6.2
MSE $_{\alpha\beta}$ (%)	1.4	0.7	1.0	0.5
MSE $_{xy}$ (%)	1.9	1.0	0.2	0.03

was a certain (small) steady-state torque tracking error in Figs. 8 and 9, this deviation is compensated in practice by the outer loop so that the speed target is met.

Additional tests have also been carried out to evaluate the performance of the conventional and proposed HCC using unchorded A6 and chorded S6 configurations, which offer larger xy inductances (see Table II) [25]. The current THD and MSE values are reflected in Table IV. The greater distortion for this S6 machine is not due to the current control, but to a rotor slot harmonic, since the number of rotor bars had been chosen for the original three-phase machine before being rewound [25]. Concerning the HCC performance, it can be concluded that, thanks

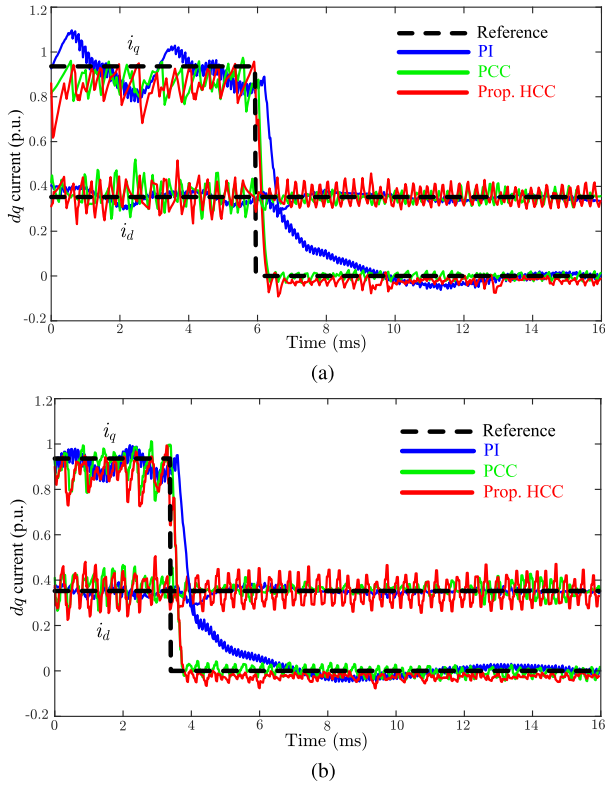


Fig. 10. dq currents when a step is applied in the q -axis current reference at 1400 r/min, in absence of outer speed control. (a) S6. (b) A6.

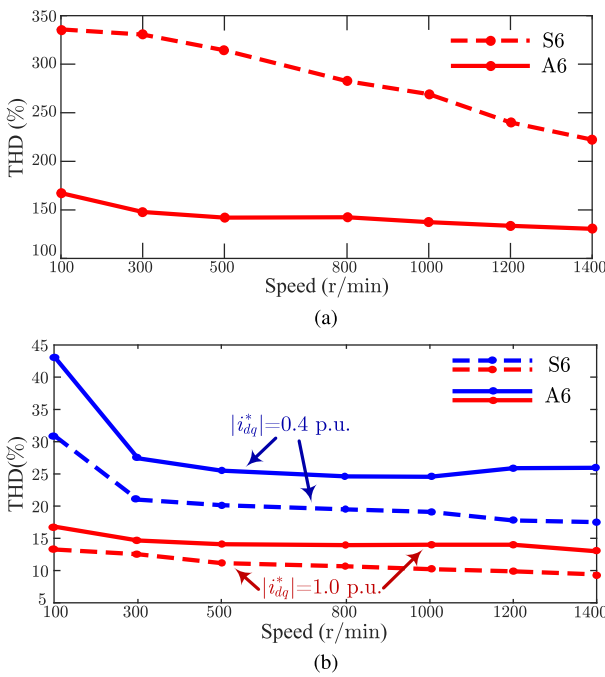


Fig. 11. Current THD versus speed for $|i_{dq}^*| = 0.4$ p.u. (blue) and $|i_{dq}^*| = 1.0$ p.u. (red) load and for S6 (dashed) and A6 (solid) when using (a) the conventional HCC or (b) the proposed HCC.

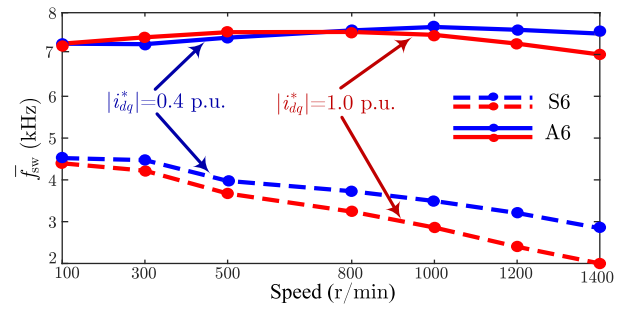


Fig. 12. Average switching frequency versus speed for $|i_{dq}^*| = 0.4$ p.u. (blue) and $|i_{dq}^*| = 1.0$ p.u. (red) load and for S6 (dashed) and A6 (solid) when using the proposed HCC.

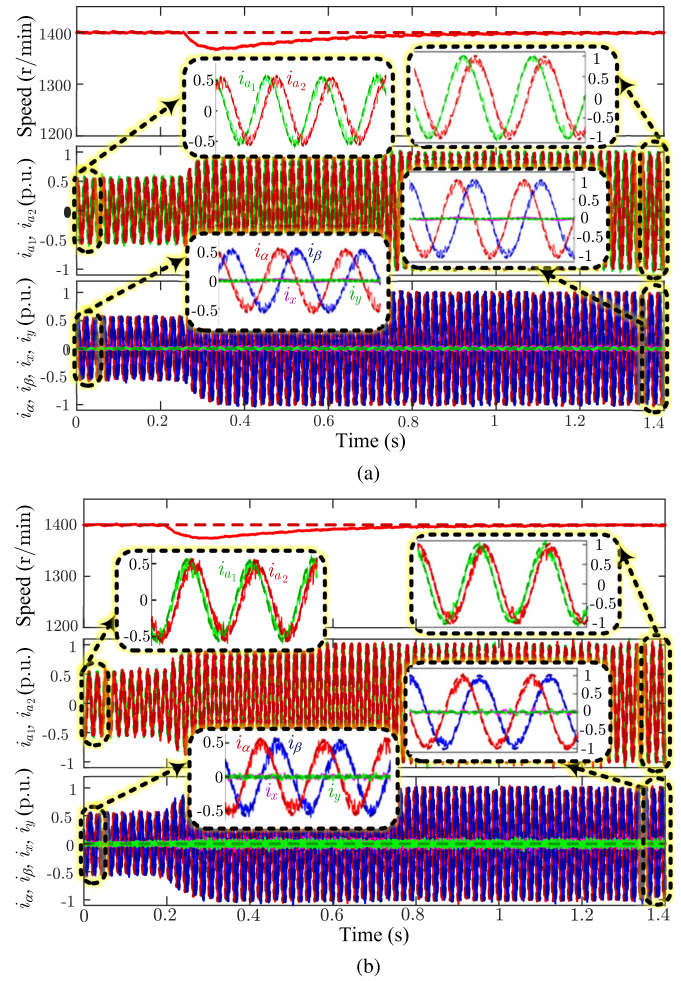


Fig. 13. Response to a load step from light load to full load at 1400 r/min when using the proposed HCC and outer speed PI control. (a) S6. (b) A6.

to the higher xy impedances, in these cases, the conventional HCC is able to provide acceptable performance but the proposed HCC is still preferred in terms of reference tracking and current distortion.

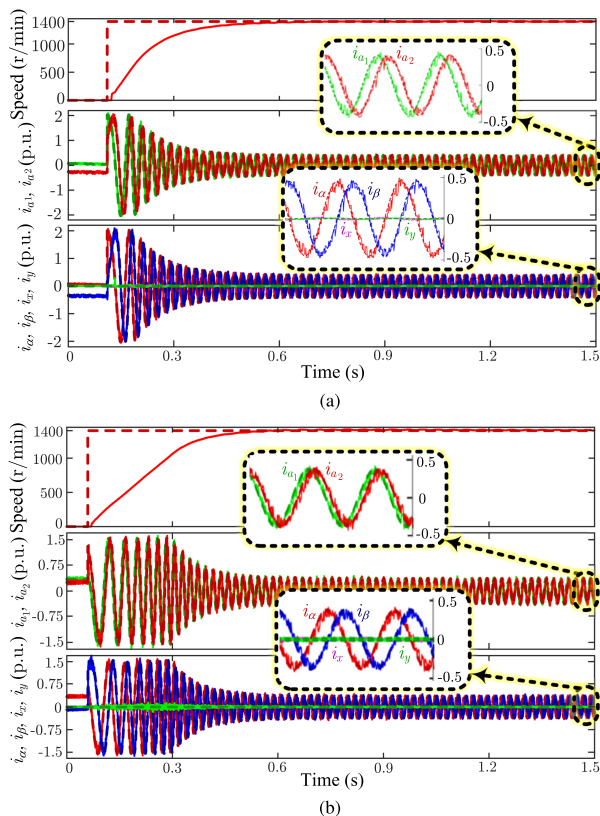


Fig. 14. Response to a speed-reference step when using the proposed HCC and outer speed PI control. (a) S6. (b) A6.

V. CONCLUSION

This article has proposed a new HCC technique, based on VSD and restrained VVs, that enhances the performance of the HCC applied to 6PIMs with S6 or A6 winding configurations. On the one hand, the conventional HCC exhibits a poor performance for 6PIMs with a substantial mismatch between the subspace impedances. This poor performance is due to the fact that the conventional HCC relies on the assumption that the relation between each phase voltage and current is a pure inductance, which is particularly far from true in 6PIMs, where the xy impedance is much smaller than the $\alpha\beta$ one. On the other hand, the proposed HCC, which decomposes the input and output signals per VSD subspaces and adequately selects the output VVs, enhances the performance of the HCC in terms of the current tracking and waveform quality, even if the xy impedance is very low. This improvement, which is the principal contribution of this article, is mainly allowed by the fact that the proposal effectively removes the xy plane from the plant model seen by the HCC by suitably handling the VSD components. In this manner, the $\alpha\beta$ current is effectively controlled in closed loop so that it follows its reference, whereas the xy voltage is nullified in open loop. Furthermore, since the xy current is not actively controlled, it naturally adapts to open-phase faults, providing reconfiguration-less tolerance. It is also worth emphasizing that the proposed HCC is parameter independent.

The experimental results have confirmed the effectiveness of the proposed technique using 6PIMs with unchorded S6 and chorded A6 windings, which have especially low xy inductances. The current THD was reduced by more than 20 times and ten times for S6 and A6, respectively, compared with the conventional HCC. In terms of the MSEs, the proposed HCC reduced them greatly for both 6PIMs, as well. On the other hand, the well-known advantages of the conventional HCC compared with PI and PCC were preserved. In transient conditions, the results also showed a good dynamic behavior. Reconfiguration-less tolerance to open-phase faults was achieved, retaining satisfactory $\alpha\beta$ current tracking and low distortion. For chorded S6 and unchorded A6 6PIMs, which offered higher xy inductances, the improvement over the conventional HCC was less remarkable, but still noticeable.

For future work, further investigation may be carried out to attain HCC with fixed switching frequency, even smaller steady-state error, lower dv/dt , or with a greater degree of control of the secondary subspaces. The last feature could be employed to provide, e.g., better disturbance compensation, increased torque density by exploiting the space harmonics or the overload capability [41], or maximum postfault load range with minimum losses [11], which may require different xy currents. The possibility of achieving further mitigation of the current distortion at low speed could be studied. Other kinds of machines, such as PMSMs with significant back-EMF harmonics, may also be addressed.

REFERENCES

- [1] E. Levi, R. Bojoi, F. Profumo, H. A. Toliyat, and S. Williamson, "Multi-phase induction motor drives—a technology status review," *IET Electric Power Appl.*, vol. 1, no. 4, pp. 489–516, Jul. 2007.
- [2] A. Salem and M. Narimani, "A review on multiphase drives for automotive traction applications," *IEEE Trans. Transport. Electrific.*, vol. 5, no. 4, pp. 1329–1348, Dec. 2019.
- [3] A. G. Yepes, O. Lopez, I. Gonzalez-Prieto, M. Duran, and J. Doval-Gandoy, "A comprehensive survey on fault tolerance in multiphase ac drives, Part 1: General overview considering multiple fault types," *Machines*, vol. 10, no. 3, 2022, Art. no. 208.
- [4] F. Barrero, M. Bermudez, M. J. Duran, P. Salas, and I. Gonzalez-Prieto, "Assessment of a universal reconfiguration-less control approach in open-phase fault operation for multiphase drives," *Energies*, vol. 12, no. 24, 2019, Art. no. 4698.
- [5] M. J. Duran, I. Gonzalez-Prieto, and A. Gonzalez-Prieto, "Large virtual voltage vectors for direct controllers in six-phase electric drives," *Int. J. Elect. Power Energy Syst.*, vol. 125, Feb. 2021, Art. no. 106425.
- [6] A. Gonzalez-Prieto, I. Gonzalez-Prieto, A. G. Yepes, M. J. Duran, and J. Doval-Gandoy, "On the advantages of symmetrical over asymmetrical multiphase AC drives with even phase number using direct controllers," *IEEE Trans. Ind. Electron.*, vol. 69, no. 8, pp. 7639–7650, Aug. 2022.
- [7] E. Levi, "FOC: Field oriented control," in *The Industrial Electronics Handbook*. Boca Raton, FL, USA: CRC, 2011, ch. 24, pp. 646–677.
- [8] H. Guzman et al., "Comparative study of predictive and resonant controllers in fault-tolerant five-phase induction motor drives," *IEEE Trans. Ind. Electron.*, vol. 63, no. 1, pp. 606–617, Jan. 2016.
- [9] M. A. Mossa, H. Echeikh, A. A. Z. Diab, H. Haes Alhelou, and P. Siano, "Comparative study of hysteresis controller, resonant controller and direct torque control of five-phase IM under open-phase fault operation," *Energies*, vol. 14, no. 5, 2021, Art. no. 1317.
- [10] H. A. Young, M. A. Perez, J. Rodriguez, and H. Abu-Rub, "Assessing finite-control-set model predictive control: A comparison with a linear current controller in two-level voltage source inverters," *IEEE Ind. Electron. Mag.*, vol. 8, no. 1, pp. 44–52, Mar. 2014.

- [11] A. G. Yepes, I. Gonzalez-Prieto, O. Lopez, M. Duran, and J. Doval-Gandoy, "A comprehensive survey on fault tolerance in multiphase AC drives, Part 2: Phase and switch open-circuit faults," *Machines*, vol. 10, no. 3, 2022, Art. no. 221.
- [12] H. A. Toliyat, "Analysis and simulation of five-phase variable-speed induction motor drives under asymmetrical connections," *IEEE Trans. Power Electron.*, vol. 13, no. 4, pp. 748–756, Jul. 1998.
- [13] F. De Belie, X. Kestelyn, and N. K. Nguyen, "Fault-tolerant optimal-current torque-controlled five-phase PMSMs with open-circuited phases: Position self-sensing operation," in *Proc. IEEE Veh. Power Propulsion Conf.*, 2014, pp. 1–6.
- [14] L. Parsa and H. A. Toliyat, "Fault-tolerant interior-permanent-magnet machines for hybrid electric vehicle applications," *IEEE Trans. Veh. Technol.*, vol. 56, no. 4, pp. 1546–1552, Jul. 2007.
- [15] S. Dwari and L. Parsa, "Fault-tolerant control of five-phase permanent-magnet motors with trapezoidal back EMF," *IEEE Trans. Ind. Electron.*, vol. 58, no. 2, pp. 476–485, Feb. 2011.
- [16] Z. Kuang, S. Wu, B. Du, H. Xu, S. Cui, and C. C. Chan, "Thermal analysis of fifteen-phase permanent magnet synchronous motor under different fault tolerant operations," *IEEE Access*, vol. 7, pp. 81466–81480, 2019.
- [17] X. Kestelyn and E. Semail, "A vectorial approach for generation of optimal current references for multiphase permanent-magnet synchronous machines in real time," *IEEE Trans. Ind. Electron.*, vol. 58, no. 11, pp. 5057–5065, Nov. 2011.
- [18] N. Bianchi, S. Bolognani, and M. D. Pre, "Impact of stator winding of a five-phase permanent-magnet motor on postfault operations," *IEEE Trans. Ind. Electron.*, vol. 55, no. 5, pp. 1978–1987, May 2008.
- [19] A. Mohammadpour, S. Sadeghi, and L. Parsa, "A generalized fault-tolerant control strategy for five-phase PM motor drives considering star, pentagon, and pentacle connections of stator windings," *IEEE Trans. Ind. Electron.*, vol. 61, no. 1, pp. 63–75, Jan. 2014.
- [20] A. Mohammadpour and L. Parsa, "Global fault-tolerant control technique for multiphase permanent-magnet machines," *IEEE Trans. Ind. Appl.*, vol. 51, no. 1, pp. 178–186, Jan./Feb. 2015.
- [21] S. Dwari and L. Parsa, "An optimal control technique for multiphase PM machines under open-circuit faults," *IEEE Trans. Ind. Electron.*, vol. 55, no. 5, pp. 1988–1995, May 2008.
- [22] Z. Chen, P. Wang, K. Liu, Z. Liu, and D. Jang, "Fixed-frequency hysteresis controller for fault-tolerant control of six-phase permanent magnet synchronous motor," in *Proc. IEEE 4th Int. Elect. Energy Conf.*, 2021, pp. 1–6.
- [23] B. P. Reddy, A. Iqbal, S. Rahman, M. Meraj, and S. Keerthipati, "Dynamic modeling and control of pole-phase modulation-based multiphase induction motor drives," *IEEE Trans. Emerg. Sel. Topics Power Electron.*, vol. 10, no. 3, pp. 3383–3394, Jun. 2022.
- [24] A. Shawier, A. Habib, M. Mamdouh, A. S. Abdel-Khalik, and K. H. Ahmed, "Assessment of predictive current control of six-phase induction motor with different winding configurations," *IEEE Access*, vol. 9, pp. 81125–81138, 2021.
- [25] A. Shawier et al., "Effect of winding design on the performance of predictive current control of six-phase induction machine-based propulsion systems," *IEEE Access*, vol. 10, pp. 80587–80599, 2022.
- [26] Y. Wu et al., "A direct model predictive control strategy with an implicit modulator for six-phase PMSMs," *IEEE Trans. Emerg. Sel. Topics Power Electron.*, vol. 11, no. 2, pp. 1291–1304, Apr. 2023.
- [27] I. Gonzalez-Prieto, M. J. Duran, J. J. Aciego, C. Martin, and F. Barrero, "Model predictive control of six-phase induction motor drives using virtual voltage vectors," *IEEE Trans. Ind. Electron.*, vol. 65, no. 1, pp. 27–37, Jan. 2018.
- [28] I. Gonzalez-Prieto, M. J. Duran, M. Bermudez, F. Barrero, and C. Martín, "Assessment of virtual-voltage-based model predictive controllers in six-phase drives under open-phase faults," *IEEE Trans. Emerg. Sel. Topics Power Electron.*, vol. 8, no. 3, pp. 2634–2644, Sep. 2020.
- [29] C.-T. Pan and T.-Y. Chang, "An improved hysteresis current controller for reducing switching frequency," *IEEE Trans. Power Electron.*, vol. 9, no. 1, pp. 97–104, Jan. 1994.
- [30] R. Ramchand, C. Patel, A. Das, K. Sivakumar, K. Gopakumar, and L. M. Patnaik, "A current error space vector based hysteresis controller with constant switching frequency and simple online boundary computation for VSI fed IM drive," in *Proc. IEEE 36th Annu. Conf. IEEE Ind. Electron. Soc.*, 2010, pp. 729–734.
- [31] L. Ren, E. Xie, Y. Zhao, and Z. Zhang, "A novel hysteresis current control scheme in synchronous dq-frame for PMSM," in *Proc. IEEE 22nd Int. Conf. Elect. Mach. Syst.*, 2019, pp. 1–6.
- [32] M. S. Abdel-Majeed, A. Shawier, A. S. Abdel-Khalik, M. S. Hamad, M. M. Sedky, and N. A. Elmally, "General current control of six-phase-based non-isolated integrated on-board charger with low order harmonic compensation," *Sustainability*, vol. 14, no. 3, 2022, Art. no. 1088.
- [33] J. Serra and A. J. M. Cardoso, "A simplified model predictive control for asymmetrical six-phase induction motors that eliminates the weighting factor," *Machines*, vol. 10, no. 12, 2022, Art. no. 1189.
- [34] W. N. W. A. Munim, M. J. Duran, H. S. Che, M. Bermúdez, I. Gonzalez-Prieto, and N. A. Rahim, "A unified analysis of the fault tolerance capability in six-phase induction motor drives," *IEEE Trans. Power Electron.*, vol. 32, no. 10, pp. 7824–7836, Oct. 2017.
- [35] G.-J. Jo and J.-W. Choi, "Gopinath model-based voltage model flux observer design for field-oriented control of induction motor," *IEEE Trans. Power Electron.*, vol. 34, no. 5, pp. 4581–4592, May 2019.
- [36] A. S. Abdel-Khalik, M. S. Abdel-Majeed, and S. Ahmed, "Effect of winding configuration on six-phase induction machine parameters and performance," *IEEE Access*, vol. 8, pp. 223009–223020, 2020.
- [37] A. G. Yepes, M. S. Abdel-Majeed, H. S. Che, A. S. Abdel-Khalik, S. Ahmed, and J. Doval-Gandoy, "DC-signal injection for stator-resistance estimation in symmetrical six-phase induction motors under open-phase fault," *IEEE Trans. Ind. Electron.*, vol. 70, no. 6, pp. 5444–5453, Jun. 2023.
- [38] A. G. Yepes, A. Vidal, J. Malvar, O. López, and J. Doval-Gandoy, "Tuning method aimed at optimized settling time and overshoot for synchronous proportional-integral current control in electric machines," *IEEE Trans. Power Electron.*, vol. 29, no. 6, pp. 3041–3054, Jun. 2014.
- [39] R. Bojoi, M. Lazzari, F. Profumo, and A. Tenconi, "Digital field-oriented control for dual three-phase induction motor drives," *IEEE Trans. Ind. Appl.*, vol. 39, no. 3, pp. 752–760, May/Jun. 2003.
- [40] A. G. Yepes, J. Doval-Gandoy, and H. A. Toliyat, "Multifrequency current control for n -phase machines including antiwindup and distortion-free saturation with full dc-bus utilization," *IEEE Trans. Power Electron.*, vol. 34, no. 10, pp. 9891–9905, Oct. 2019.
- [41] A. G. Yepes, A. Shawier, W. E. Abdel-Azim, A. S. Abdel-Khalik, S. Ahmed, and J. Doval-Gandoy, "General online current-harmonic generation for increased torque capability with minimum stator copper loss in fault-tolerant multiphase induction motor drives," *IEEE Trans. Transp. Electr.*, to be published, doi: [10.1109/TTE.2023.3244742](https://doi.org/10.1109/TTE.2023.3244742).



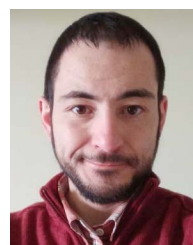
Abdullah Shawier received the B.Sc. and M.Sc. degrees in electrical engineering from Alexandria University, Alexandria, Egypt, in 2016 and 2021, respectively.

He is currently an Assistant Lecturer with the Electrical Engineering Department, Faculty of Engineering, Alexandria University. His current research interests include electric drives, multiphase machine, model predictive control, battery chargers, and power electronics.



Wessam E. Abdel-Azim received the B.Sc. degree in electrical engineering from Alexandria University, Alexandria, Egypt, in 2018.

He is currently a Teaching Assistant with the Department of Electrical, Faculty of Engineering, Alexandria University. His current research interests include electric drives, power electronics, and pulsed power applications.



Alejandro G. Yepes (Senior Member, IEEE) received the M.Sc. and Ph.D. degrees in electrical engineering from Universidade de Vigo, Vigo, Spain, in 2009 and 2011, respectively.

Since 2008, he has been with the Applied Power Electronics Technology Research Group, Universidade de Vigo. From 2016 to 2018, he was a Visiting Scholar with the Department of Electrical and Computer Engineering, Texas A&M University, College Station, TX, USA, after which he returned to Universidade de Vigo. His

research interest includes ac power conversion, with special focus, currently, on multiphase drives.



Ayman Samy Abdel-Khalik (Senior Member, IEEE) received the B.Sc. and M.Sc. degrees from Alexandria University, Alexandria, Egypt, in 2001 and 2004, respectively, and the Ph.D. degree from Alexandria University, and Strathclyde University, Glasgow, U.K., in 2009, under a dual channel program, all in electrical engineering.

He is currently a Professor with the Electrical Engineering Department, Faculty of Engineering, Alexandria University. He serves as the Editor-in-Chief of *Alexandria Engineering Journal*. He also serves as an Associate Editor of IEEE TRANSACTIONS ON INDUSTRIAL ELECTRONICS and *IET Electric Power Applications Journal*. His current research interests include electrical machine design and modelling, electric drives, energy conversion, and renewable energy.



Shehab Ahmed (Senior Member, IEEE) received the B.Sc. degree from Alexandria University in 1999, and the M.Sc. and Ph.D. degrees in electrical engineering from Texas A&M University, College Station, TX, USA, in 2000 and 2007, respectively.

He was with Schlumberger Technology Corporation, Houston, TX, USA, from 2001 to 2007, developing downhole mechatronic systems for oilfield service products. He was with Texas A&M University at Qatar from 2007 to 2018. He is currently a Professor and the Chair of the Electrical and Computer Engineering program within the CEMSE Division, King Abdullah University of Science and Technology, Thuwal, Saudi Arabia. His research interests include subsurface mechatronics, solid-state power conversion, electric machines, and drives.



Mostafa S. Hamad (Senior Member, IEEE) received the B.Sc. and M.Sc. degrees from Alexandria University, Alexandria, Egypt, in 1999 and 2003, respectively, and the Ph.D. degree from Strathclyde University, Glasgow, U.K., in 2009, all in electrical engineering.

He is currently a Professor with the Department of Electrical and Control Engineering, College of Engineering and Technology, Arab Academy for Science, Technology and Maritime Transport (AASTMT), Alexandria, Egypt. His research interests include power electronics applications in power quality, electric drives, distributed generation, HVdc transmission systems, and renewable energy.



Jesús Doval-Gandoy (Member, IEEE) received the M.Sc. degree from the Polytechnic University of Madrid, Madrid, Spain, in 1991 and the Ph.D. degree from Universidade de Vigo, Vigo, Spain, in 1999, both in electrical engineering.

He is currently a Professor and the Head of the Applied Power Electronics Technology Research Group (APET), Universidade de Vigo. His research interest includes ac power conversion.